



Effect of Ni incorporation in cobalt oxide lattice on carbon formation during ethanol decomposition reaction

Anchu Ashok^a, Anand Kumar^{b,*}, Janarthanan Ponraj^c, Said A. Mansour^c, Faris Tarlochan^a

^a Department of Mechanical and Industrial Engineering, College of Engineering, Qatar University, P.O. Box 2713, Doha, Qatar

^b Department of Chemical Engineering, College of Engineering, Qatar University, P.O. Box 2713, Doha, Qatar

^c Qatar Environment and Energy Research Institute (QEERI), Hamad Bin Khalifa University, P.O. Box 34110, Doha, Qatar



ARTICLE INFO

Keywords:
 Catalyst deactivation
 Coking
 Ethanol decomposition
 Hydrogen production
 Carbon nanotubes
 Carbon filament

ABSTRACT

In this work, we report the results of catalytic decomposition of ethanol over a porous mixed metal oxide of Ni-Co (NiCoO_2) and analyze the effect of Ni incorporation in Co_3O_4 lattice on the activity and hydrogen selectivity from ethanol decomposition reaction. In-situ FTIR analysis was conducted between 50 °C to 400 °C for both, Co_3O_4 and NiCoO_2 , catalysts to understand the reaction mechanism leading to gas phase product distribution. On cobalt surface the reaction pathway proceeds via the formation of surface ethoxy intermediate that subsequently transforms to aldehyde and acetate intermediates before decomposing to release CO_2 , H_2 and CH_4 gases at high temperature. A similar pathway is followed on NiCoO_2 surface, leading to aldehyde intermediate, which is relatively unstable and decomposes to release CO along with CH_4 and H_2 at 400 °C. The NiCoO_2 catalyst shows relatively low selectivity for CO_2 , possibly due to the unstable aldehyde species providing little acetate intermediate that decomposes to release gaseous CO_2 . The addition of Ni improves the activity for ethanol decomposition by achieving a complete ethanol conversion at 350 °C as compared to 420 °C for cobalt alone. The crystallinity, morphology and particle analysis of the spent catalyst after the reaction was studied using XRD, SEM, and TEM respectively. The XRD shows a phase change of porous NiCoO_2 to NiCo alloy, whereas SEM indicates the presence of fibrous structure on the surface with 91.7% of carbon while keeping 1:1 ratio of Ni and Co after the reaction. The detailed analysis of carbon structure using HRTEM-STEM shows the simultaneous growth of carbon nanofibers (CNFs) and multiwalled carbon nanotubes (MWCNTs) that were favored by larger and smaller crystallites respectively. A detailed mechanism of carbon deposition is also proposed.

1. Introduction

Catalytic production of hydrogen from hydrogen rich compounds of biomass is seen as an interesting topic of research due to the possibility of a carbon neutral pathway for sustained hydrogen production. Recently, hydrogen generation from ethanol gained much research attention due to its potential for on-site H_2 generation for fuel cell and other applications. Corn stover and other biomass byproducts are being studied as a source of bioethanol production [1,2]. Researchers proposed many techniques such as steam reforming, decomposition, auto reforming, and partial oxidation to produce H_2 from light alcohol [3–6]. The highly endothermic ethanol steam reforming (ESR) reaction requires high temperature and continuous flow of steam from an external source to sustain the reaction [7–10]. Ethanol partial oxidation (EPOx) is an exothermic reaction that releases energy during the reaction with low selectivity for H_2 [11–13]. However, ethanol decomposition (ED) is

an endothermic reaction but require less energy compared to the highly endothermic ESR reaction. In addition, it provides alternate routes for producing fine chemicals such as acetaldehyde, ethyl acetate, etc. along with hydrogen.

A large number of studies based on the metal catalyst (Ni, Co, Fe, La, Pt, Ru, Pd etc.) anchored on various supported oxides such as SiO_2 , La_2O_3 , ZrO_2 , TiO_2 , Al_2O_3 , MgO etc. for the ethanol decomposition reaction have been widely investigated [14–17]. Out of these, Nickel and Cobalt have been promising because of the competitive cost, ease of preparation and seemingly high conversion rate. Kumar et al. synthesized Ni using solution combustion synthesis (SCS), which was found to be selective for methane and carbon monoxide during ethanol decomposition [18]. Wang and coworkers studied the effect of Ni and Co loading over Al_2O_3 support at a decomposition temperature between 500 °C–800 °C and identified the co-production of H_2 and multi-walled carbon nanotubes (MWCNTs). They found that 600 °C is the optimum

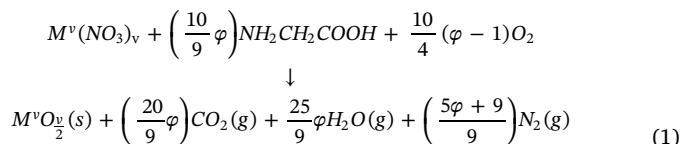
* Corresponding author.

E-mail address: akumar@qu.edu.qa (A. Kumar).

temperature to obtain the highest H₂ yield and best quality of MWCNTs [19,20]. The same group studied the ethanol decomposition over carbon supported cobalt catalyst prepared using the impregnation method [15]. Using 5% Co loading over carbon, it was possible to obtain 88% of H₂ and highly pure, low defect CNTs [15].

Sintering and coke deposition during decomposition reaction significantly reduces the activity of the catalysts at higher temperature by blocking the active sites. During ethanol decomposition reaction, the cleavage of C–C bond produces adsorbed *CH₄ and *CO species that further decompose to form carbonaceous compounds [17]. The carbonaceous species thus formed are reported to be of varying types such as carbide, amorphous, graphitic, filamentous, nanotubes, sheets and shell types, where the amount and the activity are highly influenced by preparation method, structure, reaction condition and the support used [5,14,16,21–23]. Jaime et al. reported that the physical nature of the CNT formed as a result of ethanol conversion is highly influenced by the metal particle size and decomposition conditions [16]. Zheng and coworkers concluded the existence of a critical carrier gas flow and optimum cobalt concentration below which there is no carbon nanotube formation [24].

In this work, we followed the SCS for the preparation of cobalt oxide (Co₃O₄) and Ni-Co mixed oxide (NiCoO₂) catalysts. Using SCS, it is possible to achieve porous structures, high surface area with molecular level homogeneity by utilizing water-soluble precursors to prepare the catalysts [25–27]. It has been reported that in SCS, a redox reaction between the oxidizer (metal nitrate) and reducer (fuel) provides the energy needed to start the combustion reaction that subsequently helps in calcination and crystalline phase formation [28–31]. The combustion reaction between the metal nitrate and fuel can be stoichiometrically represented as:



M^v is the metal with valency v, and φ is the fuel to oxidizer ratio. A value of $\varphi > 1$ provides fuel rich, $\varphi = 1$ stoichiometric, and $\varphi < 1$ fuel lean conditions respectively. The value of φ is expected to affect the crystallite size, oxidation state, surface area and the porosity of the solid phase synthesized [32,33]. It is expected to get metallic nanoparticle at higher φ ratio due to the presence of highly reducing atmosphere that converts the initially formed oxides to metals [26,34]. The significantly high amount of gaseous products formed during the combustion reaction can be controlled by the amount and type of fuel used, that in turn governs the porosity and the surface area [25,27,35–37]. Moreover, the combustion synthesis technique can easily be transformed into a continuous mode of synthesis for large-scale applications. As demonstrated by Mukasyan et al. [38], a combustible substrate such as cellulose paper can be utilized for this purpose to load the reactive solution and generate a stable smoldering combustion front. Under optimum conditions, the combustion front velocity will be constant that can be matched by the feed rate of cellulose paper for uninterrupted production of nanoparticles [38]. In this work, we study the mechanism of ethanol decomposition reaction on combustion synthesized cobalt oxide and Ni incorporated cobalt oxide catalysts. We also intend to investigate the driving force for the formation of different carbonaceous compound over the catalyst surface that causes the deactivation of the metal catalyst.

2. Synthesis

2.1. Synthesis of cobalt oxide

The cobalt oxide catalysts were prepared following the SCS

technique with cobalt nitrate (Co(NO₃)₂.6H₂O, metal precursor) and glycine (C₂H₅NO₂, fuel). The molar ratio of fuel to metal nitrate (φ) was maintained at 0.5 to synthesize 3 g of final nanoparticles, where each precursor was measured following the stoichiometric Eq. (1). The measured precursors were dissolved in 25 ml of deionized water to obtain a homogenous solution and were placed over a hotplate (Barnstead Thermolyne model no 46925) at 300 °C until the water evaporates, and the reactive solution is ignited. Once the mixture reaches its ignition temperature the reaction starts rapidly with a combustion flame inside the beaker. Nanoparticles thus obtained were hand ground with a mortar-pestle and filtered using a 75 µm sieve before conducting any characterization.

2.2. Synthesis of NiCoO₂ nanoparticles

NiCoO₂ was synthesized by mixing nickel nitrate (Ni(NO₃)₂.6H₂O) and cobalt nitrate (Co(NO₃)₂.6H₂O) in 1:1 M ratio and adding glycine (C₂H₅NO₂) in this mixture. The fuel to total metal nitrate ratio (φ) was kept at 0.5 that was combusted following the same procedure as adopted for the synthesis of cobalt oxide.

2.3. Experimental

Hydrogen temperature-programmed reduction (H₂-TPR) experiments were carried out on a chemisorption unit (Micrometrics Chemisorb 2750). The TPR data were collected on the synthesized catalysts under the flow of a reducing gas mixture (10% H₂ in Argon) with a flow rate of 25 sccm while heating the catalyst to 700 °C at a rate of 10 °C/min. Rigaku MiniFlexII desktop X-ray powder diffractometer was used to identify the crystallographic planes by using Cu-K α radiation of 1.54056 nm wavelength and a scan range of 10–90 degrees. SEM (Nova Nano 450, FEI) with a magnification up to 200 kx was used to study the surface morphology along with EDX for elemental analysis. The pore size distribution of the synthesized particles was analyzed using Micromeritics ASAP 2420 surface area analyzer at liquid nitrogen temperature. The surface elemental analysis and bonding configurations were studied using an X-Ray Photoelectron Spectroscopy (XPS, Kratos AXIS Ultra DLD). The size and shape study of as-synthesized particles were performed with high resolution transmission electron microscopy (FEI Talos F200X TEM coupled with EDS (FEI SuperX EDS system). The Raman profiles of the fresh and used catalysts were obtained using DXR Thermoscientific Raman spectrometer in the range of 10 cm⁻¹ to 4000 cm⁻¹ with step size of 1.5 cm⁻¹ and step time of 20 s at a wavelength of 514.53 nm.

Catalytic performance of the synthesized particles for ethanol decomposition reaction was studied in a custom-made tubular flow reactor system connected to a GC (Perkin Elmer, Clarus-580), and using an in-situ Diffused Reflectance Infrared Fourier Transform (DRIFT) spectroscopic techniques. The DRIFT studies were carried out in a Thermo Nicolet 6700 FTIR with a DRIFT reaction chamber coupled with a praying mantis optical assembly, both from Harrick Scientific. The loaded catalyst was reduced at 300 °C by the continuous flow of H₂ (100 sccm). Background spectra at different temperatures were taken by purging N₂ continuously at 100 sccm. Ethanol decomposition was conducted in the presence of ethanol at different temperatures (50–400 °C). Ethanol was allowed to pass over the sample using N₂ as a carrier gas through an ethanol bubbler kept at room temperature with a continuous flow of 100 sccm. Decomposition absorption spectra were acquired in the frequency range 600 cm⁻¹–4000 cm⁻¹ with a 4 cm⁻¹ resolution and 256 scans at each temperature.

The ethanol conversion studies were conducted using a customized tubular flow reactor consisting of a quartz tube (internal diameter of 10.5 mm, and 35 cm length) and a K-type thermocouple to measure the catalyst bed temperature. The freshly prepared catalyst powder were agglomerated to form pellets using a hydraulic press by applying a load of 25 MPa for 10 min. These agglomerates were broken up and sieved to

obtain particle size between $600\text{ }\mu\text{m}$ – 1 mm , out of which 0.4 g was loaded in the tubular reactor. The catalyst was reduced at $300\text{ }^\circ\text{C}$ in presence of H_2 for 1 h at a flow rate of 30 sccm . Once reduced, the gas flow was changed to N_2 to remove the excess H_2 residuals from the catalyst surface while the reactor was cooled down to room temperature. Thereafter ethanol was introduced to the reactor by passing 100 sccm of N_2 through an ethanol bubbler. The gaseous product from the outlet of the reactor was connected to a gas chromatography (GC) to analyze the product gases. Perkin Elmer Clarus 580 GC containing Porapak Q column was used to measure the conversion of ethanol from room temperature to $500\text{ }^\circ\text{C}$. Carboxen 1010 column was used to separate hydrogen, methane, carbon dioxide and carbon monoxide in the product mixture. The ethanol conversion was calculated using following Eq. (2):

$$\text{EtOHconv (\%)} = \left(\frac{\text{EtOH}_{\text{in}} - \text{EtOH}_{\text{out}}}{\text{EtOH}_{\text{in}}} \right) * 100 \quad (2)$$

EtOH_{in} and EtOH_{out} are the molar flow rates of ethanol at the inlet and outlet of the reactor respectively. The hydrogen selectivity was calculated using the following equation-

$$\text{H}_2 \text{ selectivity (\%)} = \frac{\text{H}_2\text{-produced}}{3 \times \text{EtOH}_{\text{converted}}} \times 100$$

3. Result and discussion

Fig. 1 shows the H_2 -TPR profile of the synthesized nanopowders at a heating rate of $10\text{ }^\circ\text{C}/\text{min}$ under 10% H_2 in Ar flow. H_2 -TPR spectrum of Co_3O_4 consists of three characteristic peaks, where the peak in the range of 390 – $415\text{ }^\circ\text{C}$ is attributed to the conversion of Co_3O_4 to CoO and

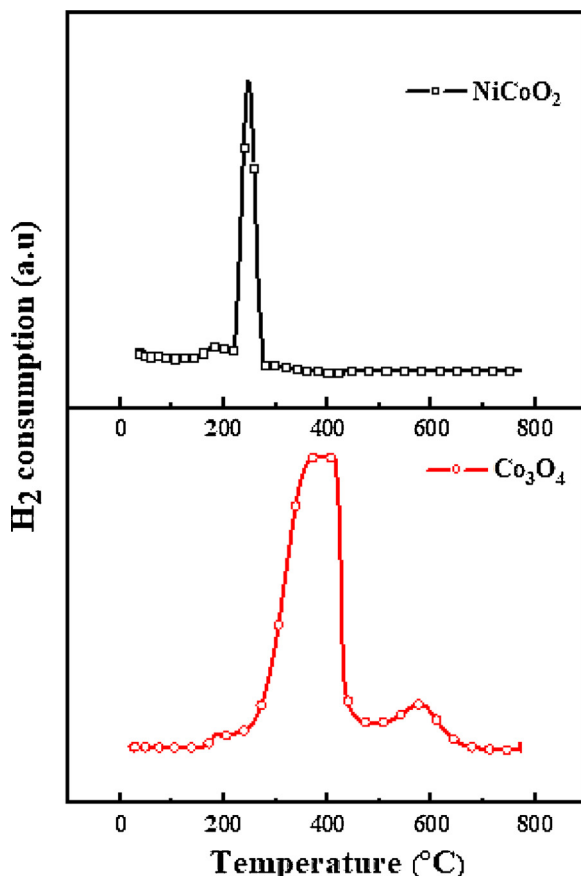


Fig. 1. H_2 -TPR profiles of Co_3O_4 and NiCoO_2 synthesized using solution combustion synthesis at $\varphi = 0.5$.

the other peak at higher temperature corresponds to the further conversion of CoO metallic Co [39]. The existence of a shake-up peak at lower temperature could be due to the presence of surface oxygen species adsorbed on the defect site of oxygen vacancy that can be easily reduced with H_2 at lower temperature [40,41]. The reduction profile of NiCoO_2 exhibit a sharp peak at $245\text{ }^\circ\text{C}$ and a small peak at $179\text{ }^\circ\text{C}$. The main peak corresponds to the complete reduction of NiCoO_2 to bimetallic NiCo form that is centered at a temperature lower than the reduction temperature of Co_3O_4 . This could be due to the sharing of oxygen atom between Ni and Co in the mixed metal oxide that improves the reducibility of the catalyst. In NiCoO_2 , both Ni and Co reduce from Ni^{2+} to Ni^0 and Co^{2+} to Co^0 simultaneously at the same temperature to produce an alloy of oxygen free Ni and Co . As otherwise, the presence of NiO and CoO separate phases would produce multiple TPR peaks at different locations corresponding to the reduction of individual oxides. On per grams basis, the TPR area for NiCoO_2 peak is 4552 unit, and for Co_3O_4 it is 9939 unit. These values indicate that Co_3O_4 required more H_2 for the complete reduction to Co as compared to the reduction of NiCoO_2 to form NiCo , which is an expected trend following the amount of oxygen present in the two oxides.

XRD profiles of as-synthesized cobalt oxide and the cobalt in presence of nickel are shown in Fig. 2a. The XRD pattern of Co_3O_4 shows the presence of a uniform face-centered cubic Co_3O_4 structure with peaks at 31.2° , 36.7° , 59.34° and 65.27° corresponding to the lattice planes of (220), (311), (511) and (440) respectively. However, the XRD spectrum of cobalt with nickel shows five distinct characteristic peaks at 36.8° , 42.82° , 61.7° , 73.9° and 77.9° attributed to the crystal planes of (111), (200), (220), (311) and (222) of cubic NiCoO_2 as per JCPDS card no. # 10-0188. These results show the solid solution alloy formation of cobalt with nickel after the proper doping without any distinct phases of Ni and Co . A 3D graphical crystal representation of NiCoO_2 in Fig. 2b shows the presence of Co^{2+} and Ni^{2+} in NaCl type of cubic structure.

The pore size distribution of Co_3O_4 and NiCoO_2 is shown in Fig. S1, which are based on N_2 adsorption-desorption isotherm. The results indicate that both Co_3O_4 and NiCoO_2 show multi-modal porous structure where most of the pores can be categorized as mesopores (20 – 500 \AA) and only a small amount of macropores ($> 500\text{ nm}$) are present. NiCoO_2 contains a sharp peak at 30 \AA and a broad peak in the range of 60 – 800 \AA indicating the existence of a wide distribution of pores. A higher peak intensity above 500 \AA for NiCoO_2 than Co_3O_4 indicates that the former contains more macropores than later. The BJH adsorption/desorption pore diameter for NiCoO_2 is $315/182\text{ \AA}$ and for Co_3O_4 the value is $139/127\text{ \AA}$.

The nanoscale composition of each element in the particles can be identified with an elemental mapping along with a high-angle annular dark-field scanning transmission electron micrograph (HAADF-STEM) as shown in Fig. 3a. The EDX mapping results (Fig. 3b–f) of Ni-doped Co indicates that Ni and Co elements are well distributed with oxygen atom without any obvious segregation of Ni or Co . In the combined elemental mapping of Ni-Co or Ni-Co-O , the uniformity can be seen throughout the structure confirming the presence of NiCoO_2 as the only major phase. It is clear that doping Ni in the Co lattice results in the formation of a well dispersed porous morphology with a solid solution formation without any individual NiO or $\text{Co}_3\text{O}_4/\text{CoO}$ nanoparticles.

The XPS of Co 2p spectrum in Co_3O_4 in Fig. 4a exhibits two major peaks at 780.5 eV and 795.6 eV corresponding to $\text{Co 2p}_{3/2}$ and $\text{Co 2p}_{1/2}$ respectively with a splitting of 15 eV . Two satellite peaks were identified at 786.4 eV and 804.5 eV which are the characteristics of cobalt oxides. The binding energies of $+3$ and $+2$ oxidation states of cobalt lie close to each other, so a deconvolution is required to identify the exact values. The deconvolution Co 2p peak at 779.5 eV (Co^{3+}) and 781.1 eV (Co^{2+}) confirm the presence of cobalt oxides in mixed oxidation state. In the NiCoO_2 sample, the Co^{3+} peak is found to be at 780.8 eV and Co^{2+} at 783 eV . It shows a positive shift in the peak position to higher binding energy with Ni alloying. Also, the Co^{3+} to Co^{2+} ($\text{Co}^{3+}/\text{Co}^{2+}$) ratio is calculated as 0.92 for Co_3O_4 , and 1.3 for NiCoO_2 .

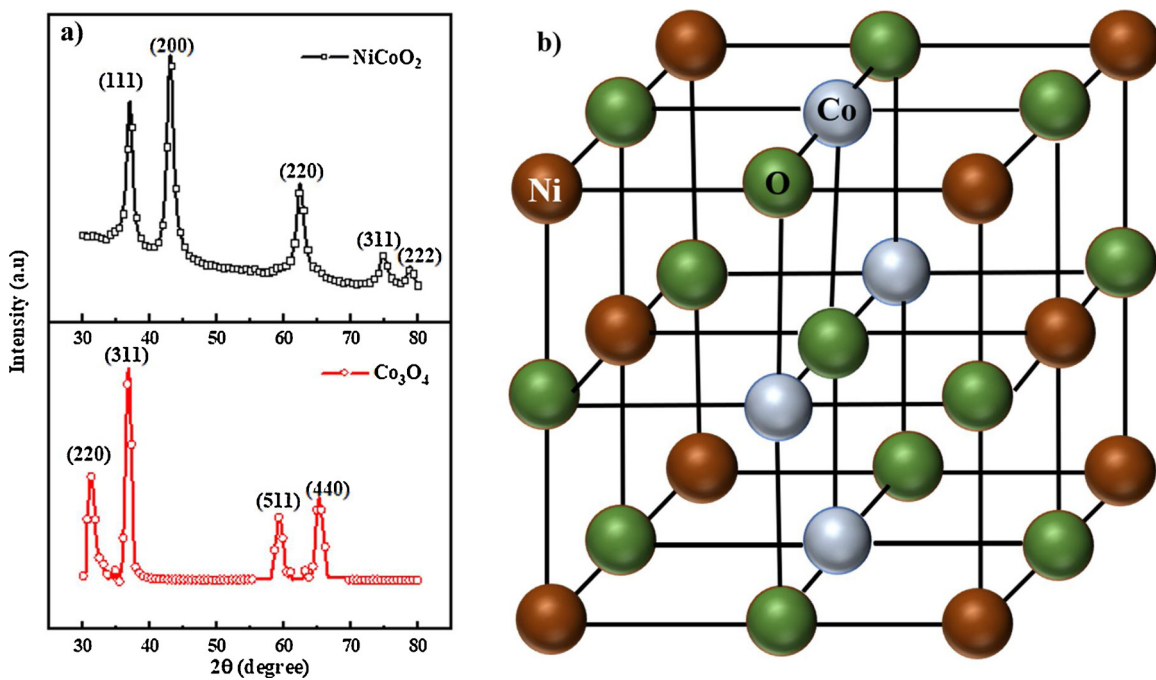


Fig. 2. XRD profile of as-synthesized a) NiCoO₂ and Co₃O₄ and b) 3D graphical crystal structure representation of cubic NiCoO₂.

indicating the presence of more Co³⁺ oxidation state on the surface compared to Co²⁺ after alloying Co with Ni. The existence of more Co³⁺ on the surface is reported to alter the performance of catalytic reactions [42]. The fitted XPS spectrum of Ni 2p in Fig. 4c represents two main peaks at 854.6 eV and 871.7 eV corresponding to Ni 2p_{3/2} and Ni 2p_{1/2} respectively. The deconvolution spectrum shows two peaks at 854.9 eV and 872 eV with an energy difference of 17.1 eV corresponding to Ni³⁺, whereas peaks centered at 856.5 eV and 874.1 eV can

be attributed to Ni²⁺ confirm the divalent nature of Ni on the solid alloy.

The deconvoluted XPS spectrum of O 1s shows three Gaussian peaks marked as O_L, O_v and O_c centered at 529.2 eV, 531.25 eV, and 532.5 eV respectively as in Fig. 4d. The O_L peak indicates the existence of metal-oxygen bonding on the lattice of Co₃O₄. The O_v peak is associated with defects or oxygen vacancies and the O_c peak is related to chemisorbed oxygen or dissociated species (O[−], O^{2−}, O₂[−]) on the surface. The O_v/O_c

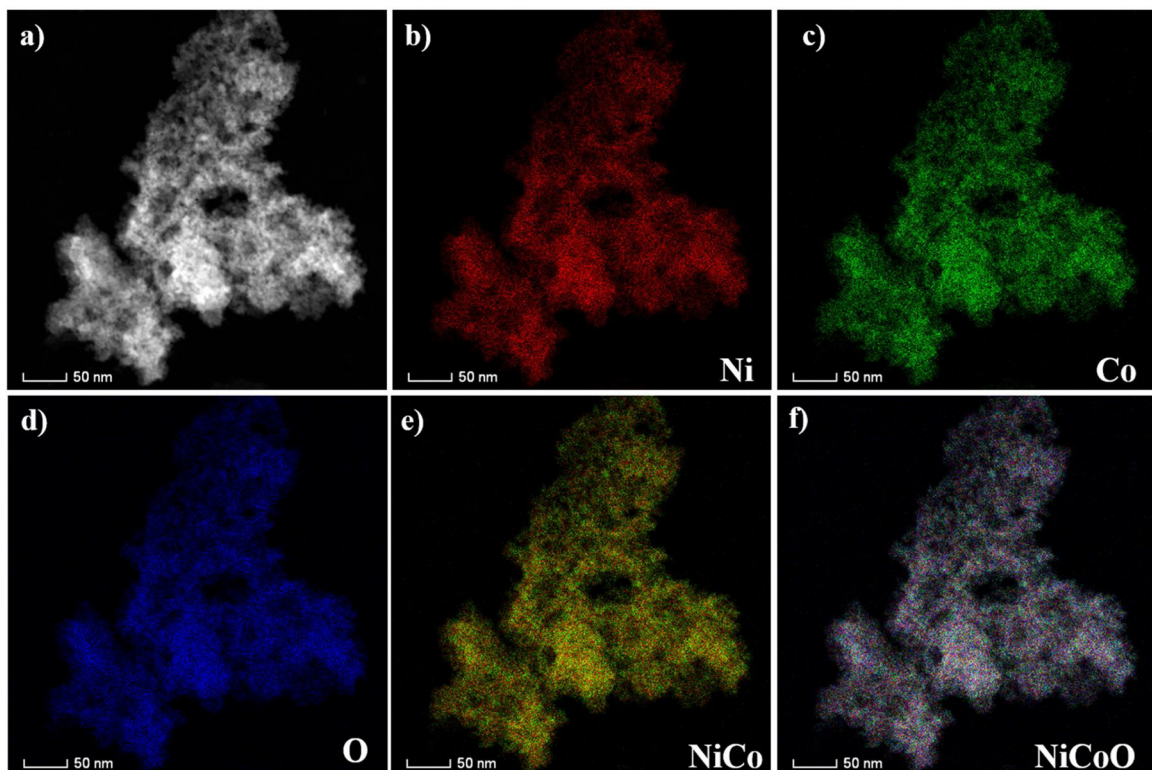


Fig. 3. HAADF-STEM image of a) Ni doped cobalt nanopowders and b–f) its corresponding elemental mapping for Ni, Co and O and its combination.

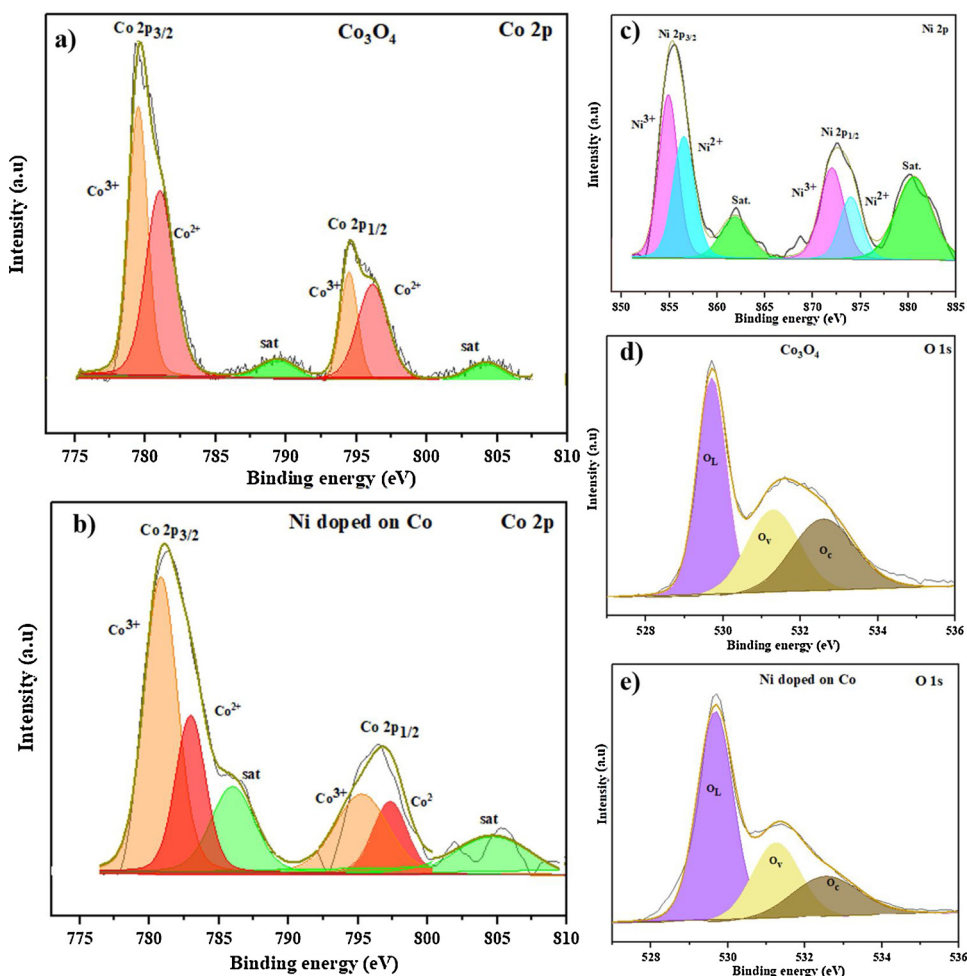


Fig. 4. XPS profile of Co 2p in a) Co_3O_4 and b) Ni doped Co c) Ni 2p in Ni doped Co and O1 s spectrum in d) Co and e) Ni doped Co.

ratio was measured as 1.287 and 0.92 for NiCoO_2 and Co_3O_4 representing the presence of more chemisorbed oxygen on the mono-metallic cobalt species. Moreover, oxygen vacancies increase and higher surface defects are expected with alloying. The mesoporous structures with more oxygen defects could improve the adsorption capacity of ethanol and allow ethanol activation at a lower temperature [14].

In situ DRIFT analysis of ethanol decomposition over SCS synthesized nickel catalyst has been previously reported [18]. Ethanol decomposition on nickel proceeds via a molecularly adsorbed ethanol ($\text{CH}_3\text{CH}_2\text{OH}^*$) on the surface to form ethoxy intermediate species ($\text{CH}_3\text{CH}_2\text{O}^*$) [18], which could form acetaldehyde with low selectivity, while predominantly favoring carbon monoxide and methane at elevated temperatures. Therefore, the primary products over the nickel catalyst after ethanol decomposition are CO and CH_4 along with H_2 . The in-situ DRIFTS analysis of ethanol decomposition over cobalt catalyst at different temperature is shown in Fig. 5. At lower temperature (50 °C and 100 °C), the vibrational peaks are similar to catalyst [18]. At 50 °C, the characteristic peak at 893, 1065, 2901 and 2972 cm^{-1} can be attributed to the surface ethoxy species and surface hydroxyl species over the catalyst surface [43,44]. The vibrational bands located at 1250 cm^{-1} ($\delta(\text{OH})$) and 1349 cm^{-1} ($\delta(\text{CH}_3)$) confirm the presence of adsorbed ethanol molecule over the surface. Above 100 °C, the intensity of acetate peaks at 1541 cm^{-1} , 1456 cm^{-1} and 1394 cm^{-1} decrease whereas the peak intensities at 2361 cm^{-1} and 2342 cm^{-1} increase, which correspond to CO_2 formation. The intermediate aldehyde peak at 1749 cm^{-1} gets stronger with an increase in temperature whereas the intensity is reported to decrease for nickel [18]. However, there is no

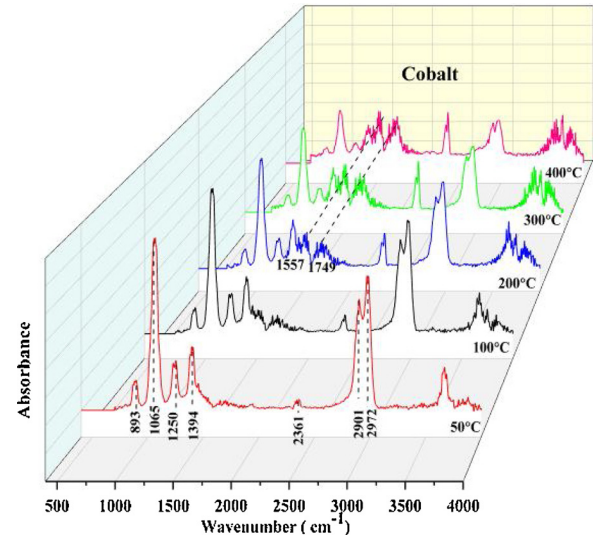


Fig. 5. In-situ FTIR spectrum of Cobalt under the decomposition of ethanol at different temperature (50–400 °C).

significant formation of CO on cobalt surface as it does not promote the conversion of aldehydes to carbon monoxide. The strong acetate band at 1557 cm^{-1} at higher temperature is from the transformation of acetaldehyde to acetic acid or ethyl acetate through the nucleophilic reaction of hydroxyl or ethoxy species with surface adsorbed aldehyde.

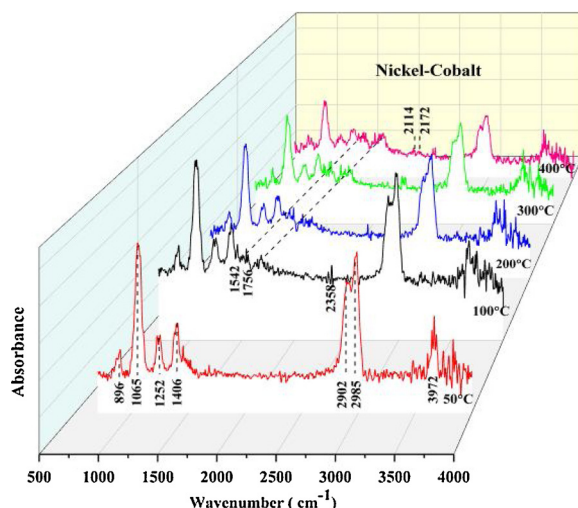


Fig. 6. In-situ FTIR spectrum of Nickel - Cobalt under the decomposition of ethanol at different temperature (50 °C – 400 °C).

Through this nucleophilic reaction of surface aldehydes, the ethoxy peaks get reduced while the acetate peak intensities increase with temperature. From the previous reports, it is clear that the primary surface intermediate from ethanol decomposition over cobalt surface is acetaldehydes which partially converts to surface acetate species that decompose releasing CO_2 and alkanes [45] as indicated by the existence of $2800\text{--}3000\text{ cm}^{-1}$ (C–H stretch), $1450\text{--}1470\text{ cm}^{-1}$ (C–H bend) and $1350\text{--}1370\text{ cm}^{-1}$ (C–H rock) vibrational bonds.

Ethanol DRIFT analysis over bimetallic NiCoO_2 at different temperatures is shown in Fig. 6. The frequency spectrum shows a similar trend as in Ni and Co at lower temperatures that are associated with the adsorption of molecular ethanol, and the formation of ethoxy species and subsequent generation of acetaldehyde intermediates. The peaks associated with the surface aldehydes at 1756 cm^{-1} has a weaker IR signal compared to the Co catalyst as in Fig. 5, and shows an improved possibility of formation of methane and carbon monoxide. The formation of carbon monoxide is confirmed through the peaks associated with 2114 cm^{-1} and 2172 cm^{-1} . In addition, there exists a small IR signal intensity at 2334 cm^{-1} associated with the release of some gaseous CO_2 . The peaks associated with CO and CO_2 at higher temperature indicate that NiCoO_2 catalyst favors the reaction pathway that is closer to Ni surface with the formation of carbon monoxide as a predominant gas phase product [18].

The catalytic activity for ethanol decomposition reaction over the reduced Co_3O_4 and NiCoO_2 catalysts are shown in Fig. S2. Prior to activity and DRIFTS analysis, the catalyst pellets were reduced by passing H_2 at 300 °C to ensure the availability of metallic or bimetallic phases of the catalyst. Cobalt shows 50% ethanol conversion at 360 °C and a complete conversion of ethanol is achieved only at 420 °C. While in case of NiCoO_2 catalyst 50% conversion takes place at 310 °C and ~100% conversion is seen at 350 °C, indicating an improvement in performance on account of doping of nickel in cobalt sites. The temperature of complete ethanol conversion is approximately 60 °C less in case of NiCoO_2 compared to the cobalt alone (420 °C). Hydrogen selectivity for NiCoO_2 and Co_3O_4 catalysts with temperature is shown in Fig. S3.a. The presence of hydrogen is detected only after the reactor temperature reaches above 250 °C for NiCoO_2 and 300 °C for Co_3O_4 . The NiCoO_2 catalyst is more selective for H_2 and shows a maximum H_2 -selectivity at 350 °C (45%) compared to 480 °C (38%) in the case of Co_3O_4 . The product distribution at T_{50} (50% ethanol conversion) is also shown in Fig. S3.b. In addition, table S1 contains detailed values at 50% and 100% ethanol conversion. The product formed during the decomposition of ethanol over NiCoO_2 shows the presence of carbon dioxide, methane and carbon monoxide. The amount of carbon monoxide decrease to its half during the complete conversion of ethanol. The main product during the decomposition of ethanol over Co_3O_4 is methane and carbon dioxide along with some trace amount of CO. From these results, it is anticipated that Co_3O_4 is more selective for CO_2 when compared to NiCoO_2 , which is consistent with the reaction pathway anticipated in DRIFT analysis.

Looking at the better performance of NiCoO_2 , we further focused on the stability and detailed material characterization of the used NiCoO_2 catalyst after the ethanol decomposition reaction. Fig. S2.b shows the stability of the NiCoO_2 catalyst at 350 °C, giving almost 100% of conversion until 14 h, thereafter it gradually decreases reaching to a value of 78% ethanol conversion after 24 h. The stability of the catalyst for the decomposition reaction is challenging due to the deactivation, possibly caused by the carbonaceous species deposited on the catalyst at a higher temperature. It should be noted that the catalyst is not supported on any refractory oxides that are known to increase the dispersion of active sites and stability of the catalyst by resisting thermal sintering. In order to increase the stability, anchoring of the active nanoparticles over inert supports can be used to resist the mobility of the nanoparticles at elevated temperatures along with providing thermal stiffness to the catalyst to prevent loss in the active surface area caused by the sintering process. It is also worth noting that the active phase is an alloy of NiCo rather than the mixed metal oxide

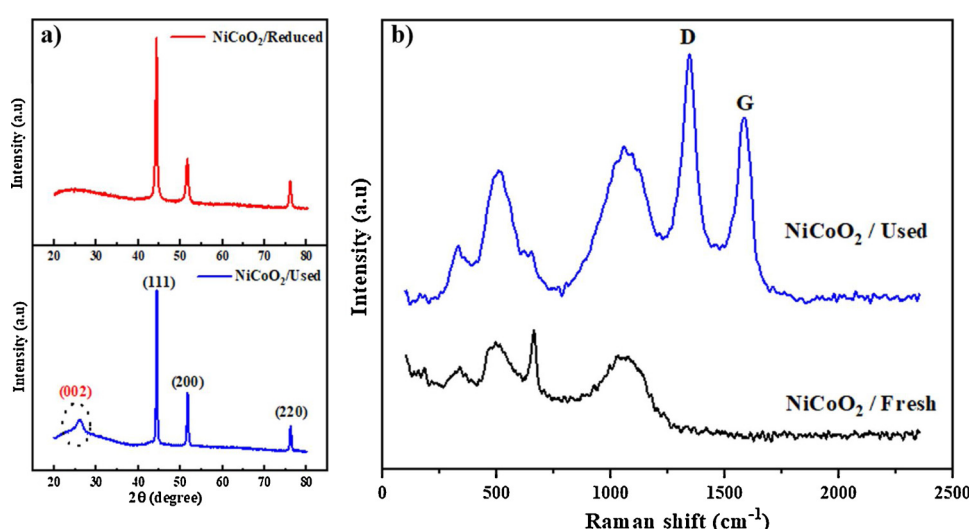


Fig. 7. a) XRD and b) Raman spectrum of NiCoO_2 catalyst after the decomposition reaction of ethanol.

NiCoO_2 as confirmed by the TPR (Fig. 1a) and the XRD of the reduced sample (Fig. 7a).

3.1. Characterization of Ni-Co catalyst after reaction

The XRD profile of NiCoO_2 after reduction in the presence of H_2 at 300 °C and after the ethanol decomposition reaction is shown in Fig. 7a. The XRD peaks corresponding to NiCoO_2 has disappeared after reduction and new peaks arise in the XRD pattern at 44.4°, 51.9° and 76.2° that correspond to JCPDS data: 01-074-5694 that indicate the change in the crystalline structure. The new peak at $2\theta = 44.36^\circ$ is formed between the pure fcc Ni(111) (JCPDS 01-1260) and Co(111) (JCPDS 15-0806) peaks that are pointed at 44.6° and 44.3° respectively. This indicates the conversion of NiCoO_2 mixed oxide to NiCo alloy after reduction and ethanol decomposition reaction. The peak shift of 43.03° in NiCoO_2 as-synthesized sample to 44.3° in NiCo confirms the formation of NiCo alloy after reduction and reaction as shown in Fig. S4. The XRD peak shift shows the changes in the cell parameter during the formation of the alloy after reduction and reaction. No characteristic peaks of any impurities or any segregated phases of Ni or Co are detected. The peak positioned at 26.06° corresponds to the (002) plane of graphite and indicates the existence of CNF/CNTs on the catalysts surface. The sharpness of the XRD peaks increases after the reaction suggesting an increase in the crystallite size after the reaction. Following the Scherrer formula, the average crystallite size calculated at 44.3° of NiCo alloy is estimated to be 70 nm and 58 nm after the reduction and reaction respectively, both of which are much larger than the crystallite size of the fresh NiCoO_2 , which is calculated to be 13 nm (Fig. 2a). The crystallite sizes calculated for all relevant peaks for the three cases follow a similar trend as shown in Table S2. This indicates that after reduction the crystallite size increases possibly due sintering at higher temperature.

The formation of NiCo alloy was further confirmed through the XPS analysis of the reduced NiCoO_2 sample as shown in Fig. S6. The Ni 2 P spectrum in Fig. S6.a consists of two characteristic peaks due to the spin orbital splitting at 852.3 eV and 869.6 eV corresponding to Ni 2 $\text{P}_{3/2}$ and Ni 2 $\text{P}_{1/2}$ that confirm the existence of Ni(0) as a dominant phase. Cobalt XPS spectrum (Co 2p) consist of two peaks at 778.9 eV (Co 2 $\text{P}_{3/2}$) and 794.3 eV (Co 2 $\text{P}_{1/2}$) with an orbital splitting of 15.4 eV implying the metallic state of cobalt in Co(0) oxidation state [46].

Raman spectrum of freshly synthesized NiCoO_2 and that of the used NiCoO_2 after the ethanol decomposition reaction are shown in Fig. 7b. The peaks in the range of 200 and 700 cm^{-1} corresponds to the vibrational peaks of metal oxides [47,48]. The Raman spectrum of the catalyst after the reaction reveals the superimposition of the features of carbon nanotubes and NiCo alloy by forming new bands and weakening the vibrational metal oxide bands through the phase transition during the heat treatment under the reduction atmosphere [49]. The two obvious peaks that are not seen in the fresh NiCoO_2 catalyst and emerge after the decomposition reaction are centered at 1334 cm^{-1} and 1586 cm^{-1} , and can be attributed to the existence of D and G bands of CNTs respectively. The D (disordered) band peaks originate from the structural defects and amorphous carbon (A_{1g} vibrational mode of C) and G band corresponds to the crystalline nature of the graphite structure (E_{2g} vibrational mode of C=C) [50,51].

The ratio of the intensities of the two peaks ($I_{\text{D}}/I_{\text{G}}$) is used to measure the defect density or the variation in the density conjugated state of the carbon material. Higher the ratio, the surface chemical modification is also expected to be higher. Generally, for pure CNTs without much surface defects the I_{D} is lower than I_{G} and the ratio is found to be less than unity. In case of the used NiCoO_2 catalyst, the $I_{\text{D}}/I_{\text{G}}$ ratio is 1.33 that indicates an increase in lattice distortion of the CNTs through the incorporation of NiCo alloy. The XRD and Raman spectrum confirm the existence of CNTs on the surface of the NiCo catalyst after the ethanol decomposition reaction.

The morphology and elemental characterization of NiCoO_2 -used catalyst is shown in Fig. 8. The SEM image gives a clear evidence of the

formation of filaments that are tangled with each other along with some agglomerated structures on the surface of the catalyst after reaction. The filaments can be in the form of carbon fibers or carbon nanotubes and the nature of the carbon can be identified using TEM. The elemental analysis in Fig. 8b shows the presence of a large amount of carbon (91.7%), whereas the oxygen content is negligible (0.64%). Also, it is clear that the Ni and Co are found approximately in the same ratio confirming a proper alloying of the catalyst as indicated in the XRD analysis.

At 100% conversion, the equivalent amount of carbon from ethanol in the inlet flow is calculated to be 0.048 mmol/min and the corresponding amount at the outlet of the reactor in the form of various carbon containing products (e.g. CO_2 , CH_4 , CO, unreacted ethanol when < 100% conversion etc.) is 0.0284 mmol/min. It is anticipated that the balance carbon, approximately 0.0198 mmol/min, is deposited on the catalyst surface as either CNT or CNF. The total carbon deposited over the catalyst is expected to be 0.2 mg/min and at this rate the carbon deposited over the catalyst after 24 h stability analysis should be 0.288 g, which is very close to the measured value of 0.298 g. The calculated value is in good agreement with the measured value, with < 4% error. This error could be associated with the presence of trace amounts of quartz wool during the weight measurement, which is placed inside the tube reactor to hold the catalyst pellets in place. The carbon formation is very clear as a significant change in catalyst bed volume can be seen during the progress of reaction as indicated in Fig. S7.

TEM micrographs of the catalyst after the reaction is shown in Fig. 9. Filaments as seen in SEM images are clear to see in Fig. 9a and particles are attached at the end of each filament. The particle size is comparatively larger than that of fresh catalyst and almost all of them possess round shape that are encapsulated inside the carbon tubes. The examination of a single particle in Fig. 9b shows the particle diameter to be approximately 60 nm, which is covered with carbonaceous deposits. A close inspection of the filaments show the presence of both carbon nanotubes (CNTs) and carbon nanofibers (CNFs) (Fig. 9c–d.). CNTs are of smaller diameter (10–15 nm) whereas the size CNF are around eight times bigger (80–100 nm) than the CNTs, with similar observations reported by other researchers [52]. The CNF structures in Fig. 9e indicates the presence of a hollow channel with orientation of graphene layers that are not parallel to the fiber axis. Whereas, in Fig. 9f the filaments with multiple graphene layers aligned parallel to the fiber axis are found to be of multi walled CNTs (CNTs). The focused image of in Fig. 9f shows the filaments with well-arranged MWCNTs having an average outer diameter of ~10 nm, inner diameter ~4 nm and 9–13 walls on each side. From the TEM, it is clear that upon reaction with ethanol, the agglomeration network of particles break to generate dispersed nanoparticles upon which the formation of CNF/CNT takes place. The particle distribution from three areas of TEM grid is shown in Fig. S8. Matching the deposited carbon structure with particle size, reveals that smaller particles (8–15 nm) that favor the formation of CNTs are relatively higher in number than the larger ones (60 to 100 nm) where CNF formation takes place. Particle size analysis under three conditions (as synthesized, reduced, and after reaction) is also presented in Table S2 as a reference.

High-angle annular dark-field imaging (HAADF) and the elemental composition analysis of various elements are shown in Fig. 10. The filaments are entangled, and the alloyed Ni-Co particles found at the end of each filament can be easily identified as bright spots. The diameter of the alloyed particles are similar to the diameter of the carbon filaments formed. The phase mapping of Ni and Co separately shows (Fig. 10b–c) that the composition of each nanoparticle is the same everywhere and no separate phase segregation of nickel or cobalt is visible. The combined image of Ni and Co (Fig. 10d) exactly match with each other, further confirming the retention of the NiCo alloyed phase even after the ethanol decomposition reaction. The existence of carbon filaments is clear from Fig. 10e, furthermore the NiCo alloy is supported with the

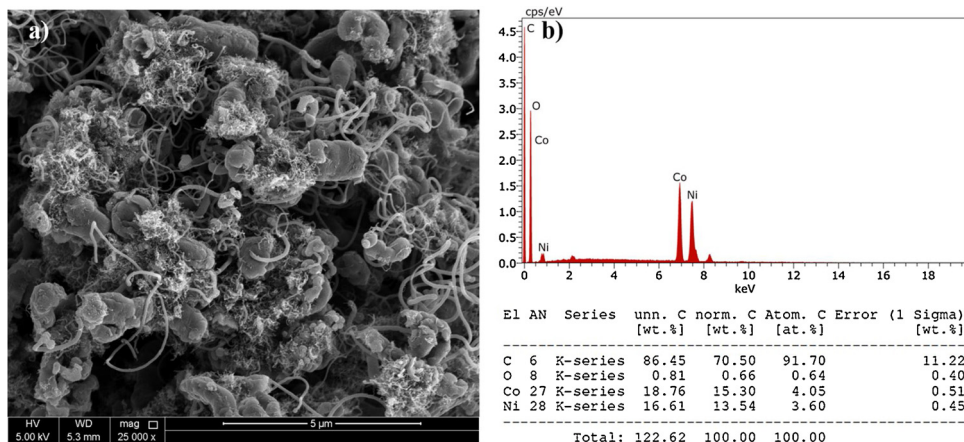


Fig. 8. a) SEM image b) EDX analysis along with the elemental composition of NiCoO_2 /Used catalysts.

carbon layer beneath it. The presence of Ni-Co over carbon tubes in Fig. 10f gives a better understanding of the existence of alloyed particle at the tip of carbon fibers.

The carbon formation was further analyzed using XPS spectrum as indicated in Fig. 11. The carbon (C 1s) spectrum of the fresh catalyst before reaction shows three peaks fitted at 283.1 eV, 285.2 eV and 863.6 eV. The peak at 283.1 eV is associated with metal-carbide bond and the well resolved peak at 285 eV corresponds to the presence adventitious carbon on the surface of the fresh catalysts after the combustion synthesis [53]. The peak at 286.7 eV comes from $\text{C}=\text{O}$, where the surface carbon is chemically bonded with the oxygen present in the metal oxide. The peak area is highest for adventitious carbon that is obvious due to the existence of unburned carbon that is formed during the solution combustion synthesis. The C 1s deconvoluted spectrum in Fig. 11b shows three fitting peaks with the sharp main peak at 284.5 eV assigned to the graphite sp^2 carbon (C–C) bond on the CNF/CNTs. The low intensity fitting peaks at 285.3 eV and 289.5 eV are attributed to the sp^3 hybridized atoms on CNT/CNFs [54]. In that, the peak at 285.1 eV may correspond to the defect in the walls of MWCNTs that are sp^3 hybridized amorphous carbon atoms [55].

Fig. 11c shows the oxygen O 1s XPS profile of the used catalyst. While comparing the oxygen spectrum of fresh catalyst in Fig. 5e, the metal-oxygen bond at 529.2 eV vanishes, as the NiCo metal oxide is directly converted into NiCo alloy after the catalyst reduction and ethanol conversion reaction. The gaussian curve fitted plot shows two

peaks, the main peak at 532.2 eV corresponds to -C–O–C- bond from ether linkages and a small peak at 536 eV revels the existence of adsorbed oxygen or water molecule on the CNF/CNTs [56–58].

3.2. Postulated mechanism for carbon formation

The continuously formed carbonaceous residue from ethanol decomposition reaction on the catalyst surface diffuses the atomic carbon to form tubular graphitic structure around the particle. The filaments formed around the nanoparticle push the active sites “up” while leaving the top of the catalyst surface available for further reaction. The structure thus formed has particle on the head and filament in the tail. The diameter of the graphitic tubular structure is similar to that of the nanoparticle size at the tip. From the TEM and SEM it can be seen that the carbon formed after the ethanol decomposition over NiCoO_2 catalyst at 350 °C in the entire area comprises of both CNFs and MWCNTs. The bigger sized CNFs (80–100 nm) and smaller sized MWCNTs (10–15 nm) are entangled together at the same time. The selectivity of CNFs and MWCNTs is influenced by the particle size of the catalyst in the reaction. CNF growth is favored by the larger particle and CNT structures were formed with smaller particles at the end. In Fig. 12, it can be seen that larger particle at the tip was tailed with CNFs and smaller particles with size 10–15 nm is ended up with MWCNTs with diameter in the same range. During the filament formation, the catalyst particle goes through a structural deformation and a pear shape (or tear

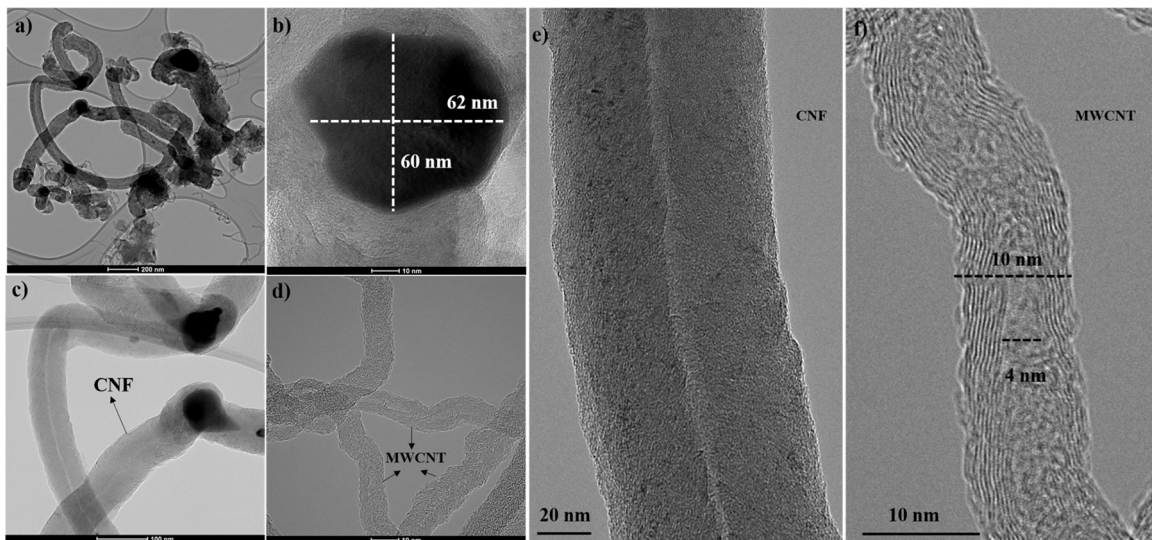


Fig. 9. TEM image of carbonaceous deposit over the catalyst and the characteristics of filaments formed.

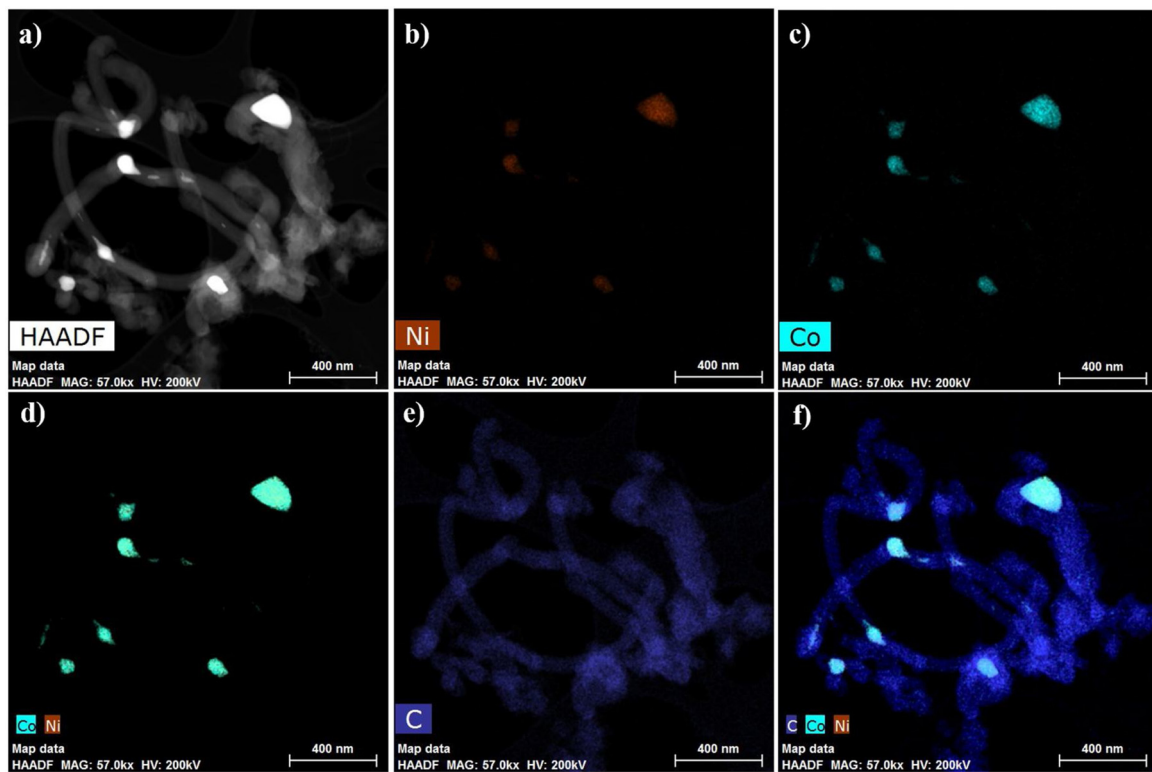


Fig. 10. a) STEM HAADF and its corresponding elemental mapping of b) Nickel c) Cobalt d) Nickel-Cobalt e) Carbon f) Nickel-Cobalt-Carbon on the used NiCoO_2 catalysts after ethanol decomposition.

drop) particle morphology pointed towards the graphite precipitation can be seen as in Fig. 12a, and the smaller particles ended with MWCNTs are almost round in morphology.

The decomposition reaction at higher temperature converts the porous smaller particles of mixed oxide into bigger alloys through the process of sintering. In absence of any refractory support, some of the smaller NiCo alloy nanoparticles are expected to sinter together at elevated temperatures following the Ostwald ripening phenomenon [59]. Once they are in contact with each other, diffusion of the particle causes neck formation and reduction of void spaces between each particle through the shrinkage of the open porosity. During the final stage, the closed pores are expected to shrink more where the grain boundary diffusion is more dominant. Finally, larger particles with better thermal stability are formed reducing the rate of sintering further. The stepwise illustration of sintering is shown in Fig. S9. From the TEM images, two sizes of catalyst nanoparticles are evident, smaller (in the range of 10–15 nm) and larger (approx. 60 nm), as a result of ethanol reaction.

Soneck et al relate the formation of hollow and filled filaments to

the rate of nucleation of the carbon and its diffusion through the particle [60]. Also, they explain the difference in the diffusion path length on the particle-carbon interface that causes the rate of carbon supply. Previous studies reported that Ni (100) is an active phase for the adsorption and conversion of hydrocarbons [61–63]. Hong et al. reported that the (100) surfaces possess the highest activation and desorption energy that leads to a strong adsorption and quick coverage of the surface with carbon [23]. Moreover, (110) and (111) have relatively weak activation and binding energies, allowing a fast diffusion of carbon atoms on the surface [23]. Ali et al. studied the formation of strongly disordered carbon nanofibers (CNFs) and quasi-perfect multi-wall carbon nanotubes (MWCNTs) owing to the presence of defective carbon and graphitic carbon over nickel particle respectively [63]. Cabero et al. and Gang et al. described the catalytic decomposition of the acetylene (catalysts/Silica) and ethanol (catalysts: $\text{Ni}/\text{Al}_2\text{O}_3$) respectively and the simultaneous synthesis of CNTs and CNFs over the catalyst [19,64]. They co-related the presence of larger particles and smaller particles with the formation of CNFs and CNTs respectively [19,64]. Based on these previous reports, it can be concluded that the

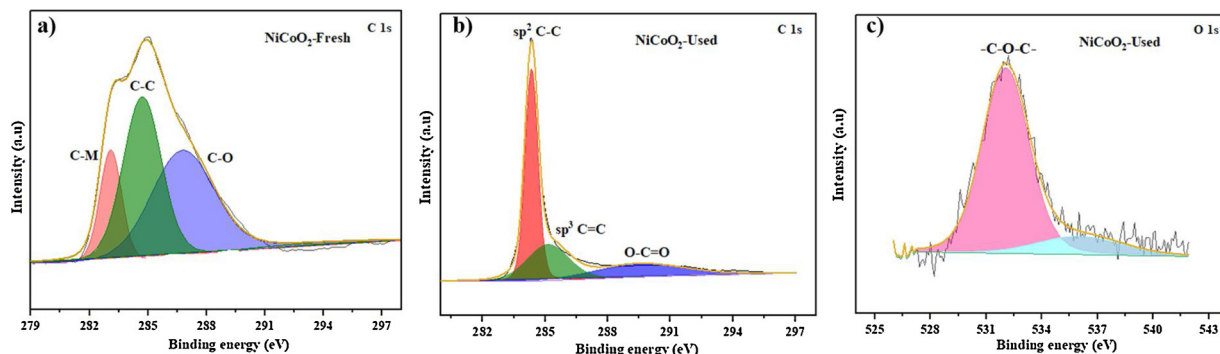


Fig. 11. XPS carbon spectrum of a) NiCoO_2 - Fresh and b) NiCoO_2 - Used catalysts and oxygen spectrum of c) NiCoO_2 - Used catalysts.

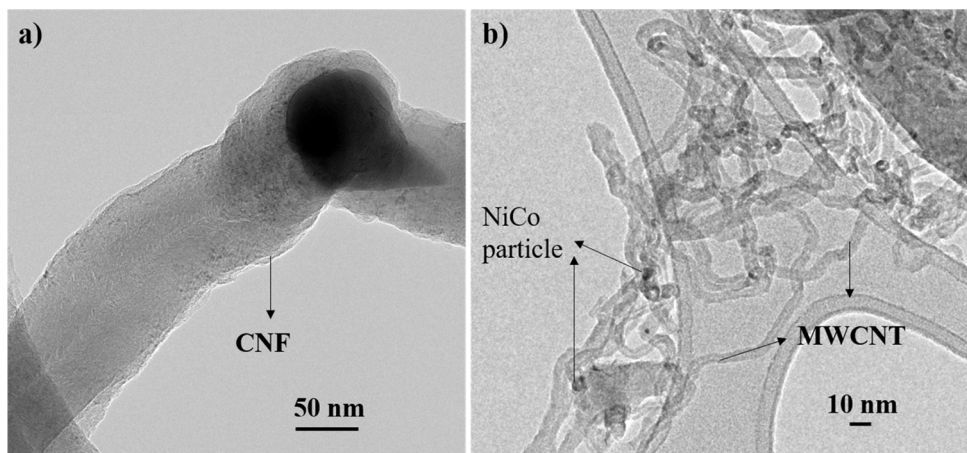


Fig. 12. a) CNF and b) MWCNT formation after the complete conversion of ethanol.

mechanism of the formation of CNFs and MWCNTs depends on the particle size, surface energy, rate of nucleation and the rate of diffusion of carbon. The nucleation of filaments needs a super-saturation of carbon atoms on the surface of the catalyst that accompanies the deformation (or reconstruction) and faceting of the carbon atoms to form graphitic layers.

For larger particles, the rate of nucleation is much slower when compared to the rate of diffusion. The supersaturated carbon atoms diffuse all over the surface of the catalyst and fill the filaments without leaving any hollow space (Fig. 13a). The ejected nucleated carbon filaments give some possible distortion with conical shape due to the

difference in the rate of excretion from metal/carbon interfaces. The ejection is faster from the outer metal-gas interface than that from the interior region of the metal because of a shorter diffusion path. Thus, the graphitic layers are ordered in conical shape along with a distortion in the shape of the metallic particle (pear shape) as reported by other researchers [21,22,65–68].

In the case of smaller particles, a larger fraction of atoms are present on the surface of the catalyst with prominent facets of {110} and {111} as compared to the bulk volume. The diffusion length on smaller particles is shorter, and the net exposed area per unit volume increases, which helps in the growth of carbon nanostructures. The nucleation in

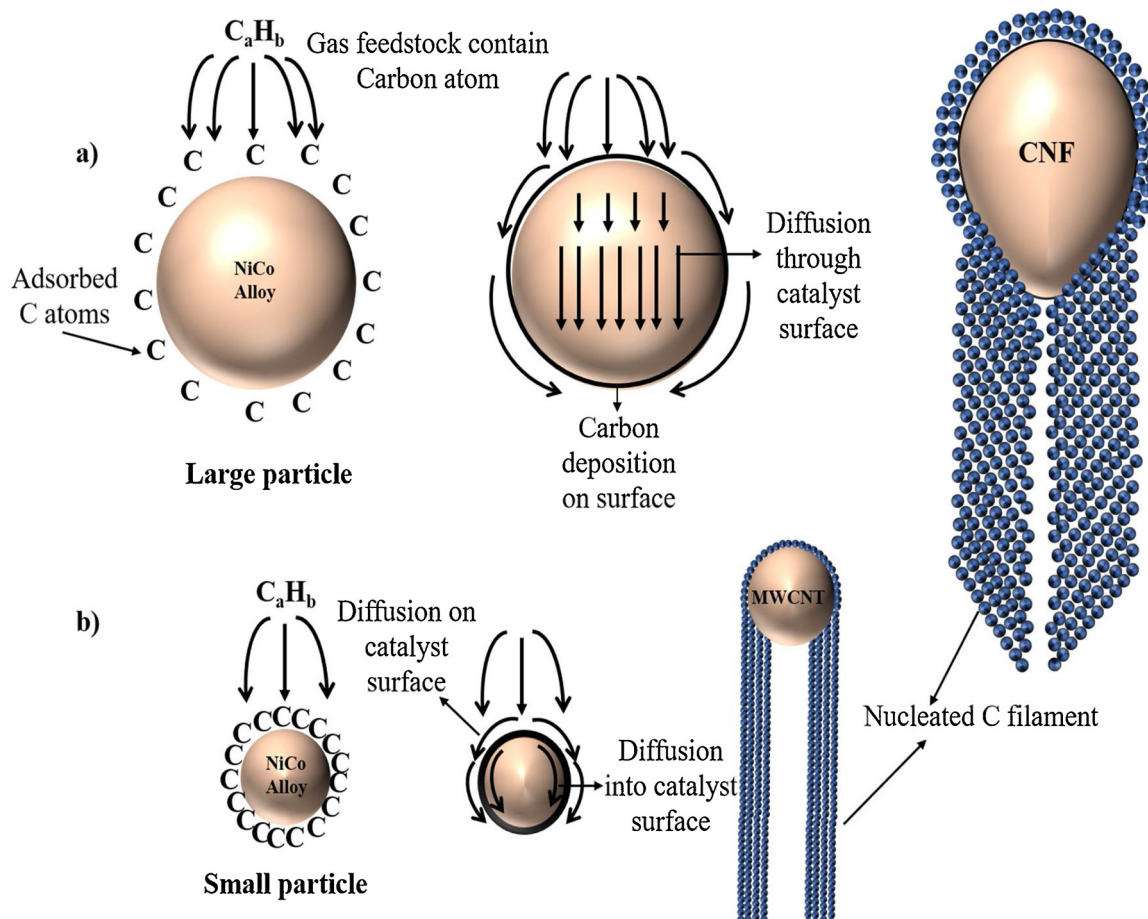
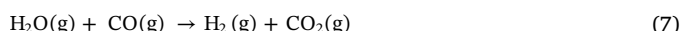
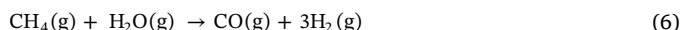
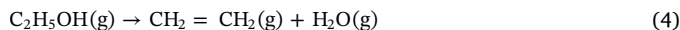
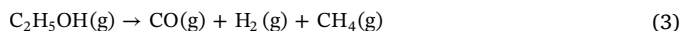


Fig. 13. Schematic diagram shows the catalyzed growth of a) CNF and b) MWCNT during the ethanol decomposition reaction.

this case is much faster on the surface than the diffusion and causes the excretion of carbon to start from the particle. As the nucleated carbon is excreted through the surface of the catalyst, the filament formed is in line with the outer diameter and leaves a gap in between. This causes the formation of hollow structure of layered graphite with multiple walls as shown in Fig. 13b. A similar observation is reported on the CNT formation in other hydrocarbons, particularly methane, reforming reactions [69,70]. The type of carbon deposition depends of many factors including the nature of active site, loading of metal in supported catalysts and the crystallite size. In general, the smaller crystallites tend to favor CNT formation and larger crystallites favor graphitic carbon deposition, nonetheless the source of carbon and the nature of metal support interaction in supported catalyst do play a significant role [69–71]. The CNT growth on large clusters of CoO-MoO on Al_2O_3 has been reported, where the MWCNT thickness increases with an increase in the crystallite size until a high metal loading resulting in particles larger than a critical dimension are obtained [72].

The possible reaction pathways during ethanol decomposition reaction are as following:



The in-situ FTIR analysis provides information about the formation of aldehyde intermediate and CO along with CO_2 as the main gas phase product at higher temperature. Based on that, the Eqs. (3), (4) and (7) are the more favorable steps involved in the ethanol decomposition on the NiCo alloy. The further decomposition of the products during ethanol decomposition thermodynamically favors carbon formation and can be expressed as:



The formation of carbon filaments in the form of CNFs and MWCNTs is more favored through Eqs. (9) and (10). As the NiCo shows a complete decomposition of ethanol at a relatively low temperature (350 °C) compared to cobalt, the Eqs. (3), (7) and (9) seem to be the preferred pathway for carbon formation [19].

3.3. Conclusion

Mixed oxide of NiCo (NiCoO_2) and cobalt oxide (Co_3O_4) were successfully synthesized using a single step solution combustion synthesis technique. The synthesized catalysts were investigated for ethanol decomposition reaction to understand the reaction mechanism and formation of carbon filaments on the surface of the catalyst. The reaction proceeds via the formation of surface aldehyde and acetate on cobalt surface that further decompose to release gaseous H_2 , CO_2 and H_2O , along with some CH_4 at higher temperature (400 °C). While the incorporation of Ni in Co lattice initially follows a similar reaction pathway but decomposes surface acetaldehyde to release CO and only small fraction of surface aldehyde is converted to acetate that subsequently decomposes releasing relatively small amount of CO_2 as high temperature. A detailed analysis of NiCo catalysts surface indicates the formation of filamentous carbon nanofibers (CNF) and multi-walled carbon nanotubes (MWCNT). CNF is found to be the primary form of carbon along with smaller amount of MWCNTs. TEM analysis reveals a good correlation between the structure of carbon and the size of catalyst nanoparticles, with smaller particles favoring MWCNT formation

and the larger particles generating CNF.

Acknowledgements

This publication was made possible by NPRP grant (NPRP8-145-2-066) from the Qatar National Research Fund (a member of Qatar Foundation). The statements made herein are solely the responsibility of the author(s). The authors also gratefully acknowledge the Center of Advances Materials (CAM) at Qatar University for carrying out XRD analysis, the Central Laboratory Unit (CLU) for services related to electron microscopy and the Gas Processing Center (GPC) for assistance in XPS analysis. The authors would like to thank Dr. Said Mansour, QEERI, for his help related to TEM and EDS analysis of samples.

Appendix A. Supplementary data

Supplementary material related to this article can be found, in the online version, at doi:<https://doi.org/10.1016/j.apcatb.2019.05.013>.

References

- [1] Y. Lin, S. Tanaka, Ethanol fermentation from biomass resources: current state and prospects, *Appl. Microbiol. Biotechnol.* 69 (2006) 627–642.
- [2] J. Sheehan, A. Aden, K. Paustian, K. Killian, J. Brenner, M. Walsh, R. Nelson, Energy and environmental aspects of using corn stover for fuel ethanol, *J. Ind. Ecol.* 7 (2003) 117–146.
- [3] F. Besenbacher, I.I. Chorkendorff, B.S. Clausen, B. Hammer, A.M. Molenbroek, J.K. Norskov, I.I. Stensgaard, Design of a surface alloy catalyst for steam reforming, *Science* 279 (1998) 1913–1915.
- [4] G. Deo, I.E. Wachs, Reactivity of supported vanadium oxide catalysts: the partial oxidation of methanol, *J. Catal.* 146 (1994) 323–334.
- [5] M. Cubeiro, J.L.G. Fierro, Partial oxidation of methanol over supported palladium catalysts, *Appl. Catal. A: Gen.* 168 (1998) 307–322.
- [6] J. Llorca, N. Homs, del Piscina, Pilar Ramirez, In situ DRIFT-mass spectrometry study of the ethanol steam-reforming reaction over carbonyl-derived Co/ZnO catalysts, *J. Catal.* 227 (2004) 556–560.
- [7] B. Zhang, X. Tang, Y. Li, Y. Xu, W. Shen, Hydrogen production from steam reforming of ethanol and glycerol over ceria-supported metal catalysts, *Int. J. Hydrogen Energy* 32 (2007) 2367–2373.
- [8] C. Diagne, H. Idriss, A. Kienemann, Hydrogen production by ethanol reforming over $\text{Rh}/\text{CeO}_2\text{-ZrO}_2$ catalysts, *Catal. Commun.* 3 (2002) 565–571.
- [9] K. Vasudeva, N. Mitra, P. Umashankar, S. Dhingra, Steam reforming of ethanol for hydrogen production: thermodynamic analysis, *Int. J. Hydrogen Energy* 21 (1996) 13–18.
- [10] F. Marino, E. Cerrella, S. Duhalde, M. Jobbagy, M. Laborde, Hydrogen from steam reforming of ethanol. Characterization and performance of copper-nickel supported catalysts, *Int. J. Hydrogen Energy* 23 (1998) 1095–1101.
- [11] Z. Wang, G. Liao, J. Wang, X. Jian, Selective oxidation of benzyl alcohol with hydrogen peroxide over reaction-controlled phase-transfer catalyst, *Catal. Commun.* 8 (2007) 1493–1496.
- [12] W. Wang, Y. Wang, Thermodynamic analysis of hydrogen production via partial oxidation of ethanol, *Int. J. Hydrogen Energy* 33 (2008) 5035–5044.
- [13] Z. Al-Hamamre, M. Hararah, Hydrogen production by thermal partial oxidation of ethanol: thermodynamics and kinetics study, *Int. J. Hydrogen Energy* 35 (2010) 5367–5377.
- [14] S.M. de Lima, A.M. Silva, U.M. Graham, G. Jacobs, B.H. Davis, L.V. Mattos, F.B. Noronha, Ethanol decomposition and steam reforming of ethanol over CeZrO_2 and Pt/CeZrO_2 catalyst: reaction mechanism and deactivation, *Appl. Catal. A: Gen.* 352 (2009) 95–113.
- [15] J. Diao, H. Wang, W. Li, G. Wang, Z. Ren, J. Bai, Effect of C-supported Co catalyst on the ethanol decomposition to produce hydrogen and multi-walled carbon nanotubes, *Physica E: Low-Dimens. Syst. Nanostruct.* 42 (2010) 2280–2284.
- [16] J. Gallego, G. Sierra, F. Mondragon, J. Barrault, C. Batiot-Dupeyrat, Synthesis of MWCNTs and hydrogen from ethanol catalytic decomposition over a $\text{Ni}/\text{La}_2\text{O}_3$ catalyst produced by the reduction of LaNiO_3 , *Appl. Catal. A: Gen.* 397 (2011) 73–81.
- [17] K.V. Manukyan, A.V. Yeghishyan, V. Danghyan, S. Rouvimov, A.S. Mukasyan, E.E. Wolf, Structural transformations of highly porous nickel catalysts during ethanol conversion towards hydrogen, *Int. J. Hydrogen Energy* 43 (2018) 13225–13236.
- [18] A. Kumar, A. Ashok, R.R. Bhosale, M.A.H. Saleh, F.A. Almomani, M. Al-Marri, M.M. Khader, F. Tarlochan, In situ DRIFTS studies on Cu, Ni and CuNi catalysts for ethanol decomposition reaction, *Catal. Lett.* 146 (2016) 778–787.
- [19] G. Wang, H. Wang, Z. Tang, W. Li, J. Bai, Simultaneous production of hydrogen and multi-walled carbon nanotubes by ethanol decomposition over $\text{Ni}/\text{Al}_2\text{O}_3$ catalysts, *Appl. Catal. B: Environ.* 88 (2009) 142–151.
- [20] G. Wang, H. Wang, W. Li, J. Bai, Preparation of hydrogen and carbon nanotubes over cobalt-containing catalysts via catalytic decomposition of ethanol, *RSC Adv.* 1 (2011) 1585–1592.

[21] R. Baker, M. Barber, P. Harris, F. Feates, R. Waite, Nucleation and growth of carbon deposits from the nickel catalyzed decomposition of acetylene, *J. Catal.* 26 (1972) 51–62.

[22] E. Boellaard, P. De Bokx, A. Kock, J.W. Geus, The formation of filamentous carbon on iron and nickel catalysts: III. Morphology, *J. Catal.* 96 (1985) 481–490.

[23] S. Hong, Y. Shin, J. Ihm, Crystal shape of a nickel particle related to carbon nanotube growth, *Jpn. J. Appl. Phys.* 41 (2002) 6142.

[24] L. Zheng, X. Liao, Y.T. Zhu, Parametric study of carbon nanotube growth via cobalt-catalyzed ethanol decomposition, *Mater. Lett.* 60 (2006) 1968–1972.

[25] A. Ashok, A. Kumar, R.R. Bhosale, F. Almomani, S.S. Malik, S. Suslov, F. Tarlochan, Combustion synthesis of bifunctional LaMO_3 ($M = \text{Cr, Mn, Fe, Co, Ni}$) perovskites for oxygen reduction and oxygen evolution reaction in alkaline media, *J. Electroanal. Chem.* 809 (2018) 22–30.

[26] A. Ashok, A. Kumar, R.R. Bhosale, M.A.H. Saleh, U.K. Ghosh, M. Al-Marri, F.A. Almomani, M.M. Khader, F. Tarlochan, Cobalt oxide nanopowder synthesis using cellulose assisted combustion technique, *Ceram. Int.* 42 (2016) 12771–12777.

[27] A. Ashok, A. Kumar, J. Ponraj, S.A. Mansour, F. Tarlochan, Single step synthesis of porous NiCoO_2 for effective electrooxidation of glycerol in alkaline medium, *J. Electrochem. Soc.* 165 (2018) J3301–J3309.

[28] A. Rogachev, A. Mukasyan, Combustion of heterogeneous nanostructural systems (review), *Combust. Shock Waves* 46 (2010) 243–266.

[29] S.T. Aruna, A.S. Mukasyan, Combustion synthesis and nanomaterials, *Curr. Opin. Solid State Mater. Sci.* 12 (2008) 44–50.

[30] A. Varma, A.S. Mukasyan, K.T. Deshpande, P. Pranda, P.R. Erri, Combustion synthesis of nanoscale oxide powders: mechanism, characterization and properties, *MRS Proceedings*, 800 (2003) AA4.1.doi:10.1557/PROC-800-AA4.1.

[31] K. Deshpande, A. Mukasyan, A. Varma, Direct synthesis of iron oxide nanopowders by the combustion approach: reaction mechanism and properties, *Chem. Mater.* 16 (2004) 4896–4904.

[32] A. Kumar, E. Wolf, A. Mukasyan, Solution combustion synthesis of metal nanopowders: Copper and copper/nickel alloys, *AIChE J.* 57 (2011) 3473–3479.

[33] A. Kumar, E. Wolf, A. Mukasyan, Solution combustion synthesis of metal nanopowders: nickel—reaction pathways, *AIChE J.* 57 (2011) 2207–2214.

[34] A. Ashok, A. Kumar, R.R. Bhosale, M.A.H. Saleh, Leo J.P. van den Broeke, Cellulose assisted combustion synthesis of porous Cu–Ni nanopowders, *RSC Adv.* 5 (2015) 28703–28712.

[35] A. Ashok, A. Kumar, R.R. Bhosale, F. Almomani, Mohd Ali H. Saleh Saad, S. Suslov, F. Tarlochan, Influence of fuel ratio on the performance of combustion synthesized bifunctional cobalt oxide catalysts for fuel cell application, *Int. J. Hydrogen Energy* 44 (2019) 436–445.

[36] A. Ashok, A. Kumar, F. Tarlochan, Preparation of nanoparticles via cellulose-assisted combustion synthesis, *Int. J. Self-Propagating High-Temperature Synth.* 27 (2018) 141–153.

[37] A. Ashok, A. Kumar, F. Tarlochan, Surface alloying in silver-cobalt through a second wave solution combustion synthesis technique, *Nanomaterials* 8 (2018) 604.

[38] A. Mukasyan, P. Dinka, Novel approaches to solution-combustion synthesis of nanomaterials, *Int. J. Self-Propagating High-Temperature Synth.* 16 (2007) 23–35.

[39] Y. Liu, H. Dai, J. Deng, S. Xie, H. Yang, W. Tan, W. Han, Y. Jiang, G. Guo, Mesoporous Co_3O_4 -supported gold nanocatalysts: highly active for the oxidation of carbon monoxide, benzene, toluene, and o-xylene, *J. Catal.* 309 (2014) 408–418.

[40] Y. Lou, L. Wang, Z. Zhao, Y. Zhang, Z. Zhang, G. Lu, Y. Guo, Y. Guo, Low-temperature CO oxidation over Co_3O_4 -based catalysts: significant promoting effect of Bi_2O_3 on Co_3O_4 catalyst, *Appl. Catal. B: Environ.* 146 (2014) 43–49.

[41] P. Li, C. He, J. Cheng, C.Y. Ma, B.J. Dou, Z.P. Hao, Catalytic oxidation of toluene over Pd/ Co_3AlO catalysts derived from hydrotalcite-like compounds: effects of preparation methods, *Appl. Catal. B: Environ.* 101 (2011) 570–579.

[42] E. Umeshbabu, G. Rajeshkhan, P. Justin, G.R. Rao, Synthesis of mesoporous NiCo_2O_4 -rGO by a solvothermal method for charge storage applications, *RSC Adv.* 5 (2015) 66657–66666.

[43] L. Mattos, F. Noronha, Hydrogen production for fuel cell applications by ethanol partial oxidation on Pt/ CeO_2 catalysts: the effect of the reaction conditions and reaction mechanism, *J. Catal.* 233 (2005) 453–463.

[44] H. Idriss, M. Scott, J. Llorca, S.C. Chan, W. Chiu, P. Sheng, A. Yee, M.A. Blackford, S.J. Pas, A.J. Hill, A phenomenological study of the metal–oxide interface: the role of catalysis in hydrogen production from renewable resources, *ChemSusChem* 1 (2008) 905–910.

[45] A. Ashok, A. Kumar, R. Bhosale, M.A.S. Saad, F. Almomani, F. Tarlochan, Study of ethanol dehydrogenation reaction mechanism for hydrogen production on combustion synthesized cobalt catalyst, *Int. J. Hydrogen Energy* 42 (2017) 23464–23473.

[46] M. Cheng, M. Wen, S. Zhou, Q. Wu, B. Sun, Solvothermal synthesis of NiCo alloy icosahedral nanocrystals, *Inorg. Chem.* 51 (2012) 1495–1500.

[47] X. Wang, X. Han, M. Lim, N. Singh, C.L. Gan, M. Jan, P.S. Lee, Nickel cobalt oxide-single wall carbon nanotube composite material for superior cycling stability and high-performance supercapacitor application, *J. Phys. Chem. C* 116 (2012) 12448–12454.

[48] Y. Yang, H. Fei, G. Ruan, C. Xiang, J.M. Tour, Efficient electrocatalytic oxygen evolution on amorphous nickel–cobalt binary oxide nanoporous layers, *ACS Nano* 8 (2014) 9518–9523.

[49] C.F. Windisch Jr., K.F. Ferris, G.J. Exarhos, Synthesis and characterization of transparent conducting oxide cobalt–nickel spinel films, *J. Vac. Sci. Technol. A: Vac. Surf. Films* 19 (2001) 1647–1651.

[50] A. Das, S. Pisana, B. Chakraborty, S. Piscanec, S. Saha, U. Waghmare, K. Novoselov, H. Krishnamurthy, A. Geim, A. Ferrari, Monitoring dopants by Raman scattering in an electrochemically top-gated graphene transistor, *Nat. Nanotechnol.* 3 (2008) nnano. 2008.67.

[51] L. Wang, Z. Sofer, J. Luxa, M. Pumera, Nitrogen doped graphene: influence of precursors and conditions of the synthesis, *J. Mater. Chem. C* 2 (2014) 2887–2893.

[52] P. Serp, M. Corrias, P. Kalck, Carbon nanotubes and nanofibers in catalysis, *Appl. Catal. A: Gen.* 253 (2003) 337–358.

[53] K. Song, Y. Lee, M.R. Jo, K.M. Nam, Y. Kang, Comprehensive design of carbon-encapsulated Fe_3O_4 nanocrystals and their lithium storage properties, *Nanotechnology* 23 (2012) 505401.

[54] R.A. Moraes, C.F. Matos, E.G. Castro, W.H. Schreiner, M.M. Oliveira, A.J. Zarbin, The effect of different chemical treatments on the structure and stability of aqueous dispersion of iron-and iron oxide-filled multi-walled carbon nanotubes, *J. Braz. Chem. Soc.* 22 (2011) 2191–2201.

[55] S. Nesov, P. Korusenko, S. Povoroznyuk, V. Bolotov, E. Knyazev, D. Smirnov, Effect of carbon nanotubes irradiation by argon ions on the formation of $\text{SnO}_{2-x}/\text{WCNTs}$ composite, *Nucl. Instrum. Methods Phys. Res. B: Beam Interact. Mater.* At. 410 (2017) 222–229.

[56] R. Larciprete, P. Lacovig, S. Gardonio, A. Baraldi, S. Lizzit, Atomic oxygen on graphite: chemical characterization and thermal reduction, *J. Phys. Chem. C* 116 (2012) 9900–9908.

[57] D. Rosenthal, M. Ruta, R. Schlägl, L. Kiwi-Minsker, Combined XPS and TPD study of oxygen-functionalized carbon nanofibers grown on sintered metal fibers, *Carbon* 48 (2010) 1835–1843.

[58] I.M. Patil, M. Lokanathan, B. Ganesan, A. Swami, B. Kakade, Carbon nanotube/boron nitride nanocomposite as a significant bifunctional electrocatalyst for oxygen reduction and oxygen evolution reactions, *Chem. Eur. J.* 23 (2017) 676–683.

[59] T.W. Hansen, A.T. DeLaRiva, S.R. Challa, A.K. Datye, Sintering of catalytic nanoparticles: particle migration or Ostwald ripening? *Acc. Chem. Res.* 46 (2013) 1720–1730.

[60] J. Snoeck, G. Froment, M. Fowles, Filamentous carbon formation and gasification: thermodynamics, driving force, nucleation, and steady-state growth, *J. Catal.* 169 (1997) 240–249.

[61] H.S. Bengaard, J.K. Nørskov, J. Sehested, B. Clausen, L. Nielsen, A. Molenbroek, J. Rostrup-Nielsen, Steam reforming and graphite formation on Ni catalysts, *J. Catal.* 209 (2002) 365–384.

[62] F. Zaera, An organometallic guide to the chemistry of hydrocarbon moieties on transition metal surfaces, *Chem. Rev.* 95 (1995) 2651–2693.

[63] A. Rinaldi, J. Tessonnier, M.E. Schuster, R. Blume, F. Girsgsdies, Q. Zhang, T. Jacob, S.B. Abd Hamid, D.S. Su, R. Schlägl, Dissolved carbon controls the initial stages of nanocarbon growth, *Angew. Chem. Int. Ed.* 50 (2011) 3313–3317.

[64] M. Perez-Cabero, I. Rodriguez-Ramos, A. Guerrero-Ruiz, Characterization of carbon nanotubes and carbon nanofibers prepared by catalytic decomposition of acetylene in a fluidized bed reactor, *J. Catal.* 215 (2003) 305–316.

[65] E. Tracz, R. Scholz, T. Borowiecki, High-resolution electron microscopy study of the carbon deposit morphology on nickel catalysts, *Appl. Catal.* 66 (1990) 133–147.

[66] H. Cui, X. Yang, H.M. Meyer, L.R. Baylor, M.L. Simpson, W.L. Gardner, D.H. Lowndes, L. An, J. Liu, Growth and properties of Si–N–C–O nanocones and graphitic nanofibers synthesized using three-nanometer diameter iron/platinum nanoparticle-catalyst, *J. Mater. Res.* 20 (2005) 850–855.

[67] S. Takenaka, S. Kobayashi, H. Ogihara, K. Otsuka, Ni/ SiO_2 catalyst effective for methane decomposition into hydrogen and carbon nanofiber, *J. Catal.* 217 (2003) 79–87.

[68] P. Tesner, E. Robinovich, I. Rafalkes, E. Arefieva, Formation of carbon fibers from acetylene, *Carbon* 8 (1970) 435–442.

[69] K.P. De Jong, J.W. Geus, Carbon nanofibers: catalytic synthesis and applications, *Catal. Rev. Res.* 42 (2000) 481–510.

[70] U. Ashik, W.W. Daud, J. Hayashi, A review on methane transformation to hydrogen and nanocarbon: Relevance of catalyst characteristics and experimental parameters on yield, *Renew. Sustain. Energy Rev.* 76 (2017) 743–767.

[71] M. Dresselhaus, Nanotechnology: new tricks with nanotubes, *Nature* 391 (1998) 19–20.

[72] K. Lee, W. Yeoh, S. Chai, S. Ichikawa, A.R. Mohamed, Catalytic decomposition of methane to carbon nanotubes and hydrogen: the effect of metal loading on the activity of CoO–MoO₃/Al₂O₃ catalyst, *Fullerenes Nanotubes Carbon Nanostruct.* 21 (2013) 158–170.